

Pyramid wavefront sensor using a sequential operation method

KAINAN YAO,^{1,2,3} JIANLI WANG,^{1,*} XINYUE LIU,¹ HONGWEN LI,¹ MINGHAO WANG,¹
BOCHUAN CUI,^{1,2} AND SHUHAI YU¹

¹Changchun Institute of Optics, Fine Mechanics and Physics, Chinese Academy of Sciences, Changchun, Jilin 130033, China

²University of China Academy of Sciences, Beijing 100049, China

³e-mail: yaokainan001@126.com

*Corresponding author: wangjianli@ciomp.ac.cn

Received 28 January 2015; revised 22 March 2015; accepted 26 March 2015; posted 27 March 2015 (Doc. ID 232678); published 21 April 2015

The pyramid wavefront sensor is a novel slope wavefront sensor that is similar to the Foucault knife-edge test. In this paper, we describe a sequential operation method that can be realized using a micromirror array. The goal of this paper is to discuss the possibility and analyze the features of the method. Geometrical optics calculations are described first to illustrate the principle of the method. Then, more exact diffraction calculations are provided that illustrate the method being equivalent to the pyramid sensor in principle but with a weak diffraction effect. Numerical simulations are also provided to verify the feasibility of using a nonmodulation method in the closed-loop system. © 2015 Optical Society of America

OCIS codes: (010.1080) Active or adaptive optics; (010.7350) Wave-front sensing.

<http://dx.doi.org/10.1364/AO.54.003894>

1. INTRODUCTION

The wavefront sensor is one of the main components of the adaptive optics system used for detecting wavefront aberration [1,2]. The pyramid wavefront sensor (PWFS) is a novel slope sensor that was proposed by Ragazzoni in 1996 [3]. It has been successfully used in the adaptive optics system of large astronomical telescopes. The performance of the PWFS on the sky objects has been reported [4–6]. It possesses the advantages of high sensitivity in closed-loop operation, good characteristics of variable gain, and adjustable sampling in real time. The PWFS is an attractive option for next generation astronomical adaptive optics systems compared with the Shack–Hartmann wavefront sensor [7,8]. It also acts as a new element in the multilayer conjugate adaptive optics system to solve the problems related with limited field of view [9]. The capability of PWFS to phase and align segmented mirrors has also been described in [10].

In this paper, we describe a sequential operation approach of PWFS (SPWFS). Compared with the wavefront sensing method proposed by Babcock in [11] and reflective pyramid sensor [12], the energy from three quadrants can be utilized by SPWFS. Our analysis shows that SPWFS has some advantages compared with PWFS. First, owing to the reflection micromirror array used, SPWFS can be used in a broadband optical system easily, without a specific achromatic design. Second, the detection element with one-fourth pixels of SPWFS can realize the same wavefront resolution as PWFS, which means higher

uniformity of sensitivity and lower cost, especially for the APD array. Third, the relay system design can be simplified. Fourth, SPWFS has a weaker diffraction effect and smoother light energy distribution. The goal of this paper is to discuss the feasibility and to analyze the features of the method. Geometrical optics calculations are described first to show that the principle of SPWFS is equivalent to that of the pyramid wavefront sensing approach. Then, more exact diffraction calculations and numerical simulations show that nonmodulation SPWFS is feasible for closed-loop adaptive optics systems. At the end of the paper, some considerations for applying SPWFS into a practical system are also discussed.

2. GEOMETRICAL OPTICS DESCRIPTION OF THE SPWFS

The PWFS with cycle modulation is composed of a four-sided pyramid prism with its vertex at the nominal focal point of the system to divide the focus spot into four beams, as shown in Fig. 1(a).

It can be seen in Fig. 1(b) that three quadrants are masked for each beam on the focus plane.

The signal is computed for each subaperture with the following formula (similar to a quad-cell signal):

$$S_x(x, y) = \frac{(I_1(x, y) + I_4(x, y)) - (I_2(x, y) + I_3(x, y))}{I_1(x, y) + I_2(x, y) + I_3(x, y) + I_4(x, y)}, \quad (1)$$

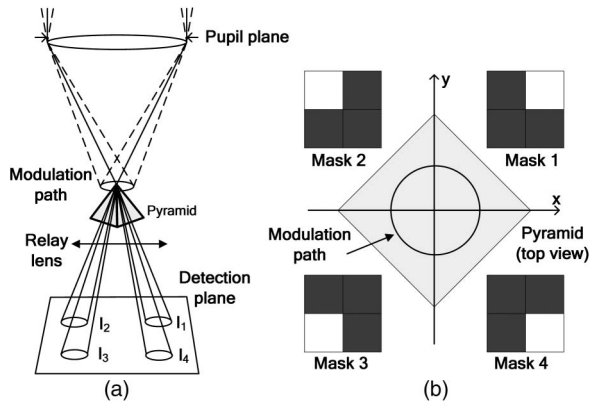


Fig. 1. Schematic diagram of PWFS.

$$S_y(x, y) = \frac{(I_1(x, y) + I_2(x, y) - I_3(x, y) + I_4(x, y))}{I_1(x, y) + I_2(x, y) + I_3(x, y) + I_4(x, y)}. \quad (2)$$

In the case of a circular tip-tilt modulation with the amplitude larger than the local tilt of the aberrated wavefront of $w(x, y)$, geometrical optics calculations show that [13]

$$\frac{\partial w(x, y)}{\partial x} \propto \sin\left(\frac{\pi}{2} S_x(x, y)\right), \quad (3)$$

$$\frac{\partial w(x, y)}{\partial y} \propto \sin\left(\frac{\pi}{2} S_y(x, y)\right). \quad (4)$$

This shows that the local tilt of wavefront is in proportion with the output signal of the PWFS, if the wavefront aberration is small enough.

The schematic diagram of the SPWFS described in this paper is shown in Fig. 2.

As a replacement for the pyramid prism, a micromirror array that consists of at least 2×2 tip-tilt mirrors is placed on the focus plane of the system. If there is no tilted micromirror, all the light will be reflected onto the detection plane. The SPWFS divides one wavefront sensing cycle into four steps and a quarter of the micromirror tilts in each step. In other words, the light that comes from three quadrants will be detected, and one quadrant is discarded.

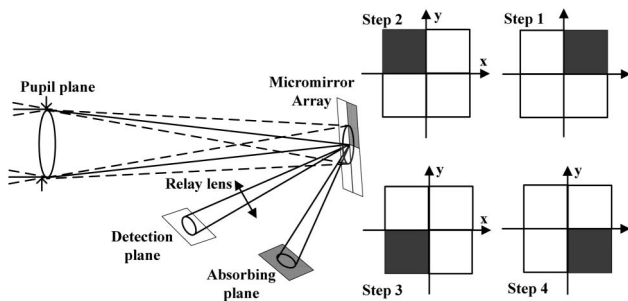


Fig. 2. Schematic diagram of SPWFS.

The output signal of SPWFS can be computed by

$$S'_x(x, y) = \frac{3 \times [(I_{\text{step}2}(x, y) + I_{\text{step}3}(x, y)) - (I_{\text{step}1}(x, y) + I_{\text{step}4}(x, y))]}{I_{\text{step}1}(x, y) + I_{\text{step}2}(x, y) + I_{\text{step}3}(x, y) + I_{\text{step}4}(x, y)}, \quad (5)$$

$$S'_y(x, y) = \frac{3 \times [(I_{\text{step}3}(x, y) + I_{\text{step}4}(x, y)) - (I_{\text{step}1}(x, y) + I_{\text{step}2}(x, y))]}{I_{\text{step}1}(x, y) + I_{\text{step}2}(x, y) + I_{\text{step}3}(x, y) + I_{\text{step}4}(x, y)}. \quad (6)$$

Equations (3) and (4) are also true for $S'_x(x, y)$ and $S'_y(x, y)$ with uncomplicated geometrical analysis. So it can be seen that the principle of SPWFS is equivalent to PWFS in geometrical optics analysis.

There are three salient advantages in SPWFS based on the geometrical optics model. First, owing to the sequential operation approach, the detection element of SPWFS only needs to accommodate one pupil image instead of the four pupil images needed by PWFS, which means that no more than one-fourth of the pixels can realize the same wavefront resolution as PWFS. Second, the relay system design can be simplified comparing with PWFS because only one image of the pupil needs to be relayed. For the PWFS, four images must be relayed from the pyramid to the camera, and thus the lens system quality must be high enough over a wider field of view. Third, a reflective mirror array will not introduce any chromatic dispersion if used in a broadband optical system, whereas achromatic design is necessary for PWFS.

3. DIFFRACTION THEORY

It has been shown that a PWFS without any modulation holds many advantages and can be used in the closed-loop adaptive optics system [14]. So, the nonmodulation SPWFS and PWFS are concerned in the following analysis. The optical diagram of SPWFS is shown in Fig. 3.

The complex amplitude in the pupil plane is defined as

$$E_1(x, y) = u_0 \exp\left[i\frac{2\pi}{\lambda} \varphi(x, y)\right] P, \quad (7)$$

where u_0 is the amplitude, $\varphi(x, y)$ is the phase, P is the aperture function, and λ is the wavelength. The complex amplitude on the micromirror array plane is

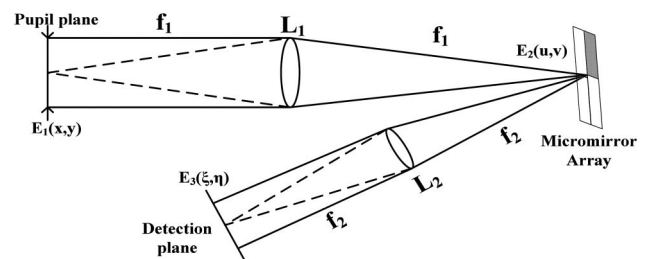


Fig. 3. Optical diagram of nonmodulation SPWFS.

$$E_2(u, v) = \frac{1}{\lambda f_1} \text{FT}[E_1(x_1, y_1)]_{(f_{x1}=\frac{u}{\lambda f_1}, f_{y1}=\frac{v}{\lambda f_1})}, \quad (8)$$

where f_1 is the focal length of L1 in Fig. 3. The phase mask of the SPWFS in steps 1–4 can be expressed by the following function:

$$\begin{aligned} \Phi_{\text{step1}} &= 1 - \frac{1}{4}[1 + \text{sgn}(u)\text{sgn}(v) + \text{sgn}(u) + \text{sgn}(v)] \\ &= \frac{3}{4} - \frac{1}{4}\text{sgn}(u)\text{sgn}(v) - \frac{1}{4}\text{sgn}(u) - \frac{1}{4}\text{sgn}(v), \end{aligned} \quad (9)$$

$$\begin{aligned} \Phi_{\text{step2}} &= 1 - \frac{1}{4}[1 - \text{sgn}(u)\text{sgn}(v) - \text{sgn}(u) + \text{sgn}(v)] \\ &= \frac{3}{4} + \frac{1}{4}\text{sgn}(u)\text{sgn}(v) + \frac{1}{4}\text{sgn}(u) - \frac{1}{4}\text{sgn}(v), \end{aligned} \quad (10)$$

$$\begin{aligned} \Phi_{\text{step3}} &= 1 - \frac{1}{4}[1 + \text{sgn}(u)\text{sgn}(v) - \text{sgn}(u) - \text{sgn}(v)] \\ &= \frac{3}{4} - \frac{1}{4}\text{sgn}(u)\text{sgn}(v) + \frac{1}{4}\text{sgn}(u) + \frac{1}{4}\text{sgn}(v), \end{aligned} \quad (11)$$

$$\begin{aligned} \Phi_{\text{step4}} &= 1 - \frac{1}{4}[1 - \text{sgn}(u)\text{sgn}(v) + \text{sgn}(u) - \text{sgn}(v)] \\ &= \frac{3}{4} + \frac{1}{4}\text{sgn}(u)\text{sgn}(v) - \frac{1}{4}\text{sgn}(u) + \frac{1}{4}\text{sgn}(v), \end{aligned} \quad (12)$$

where $\text{sgn}(u) = \begin{cases} 1 & u > 0 \\ -1 & u < 0 \end{cases}$. The complex amplitude on the detection plane is as follows:

$$\begin{aligned} E_3^n(\xi, \eta) &= \frac{1}{\lambda f_2} \text{FT}[E_2(u_1, v_1)\Phi_{\text{step}n}(u_1, v_1)]_{(f_{u1}=\frac{\xi}{\lambda f_2}, f_{v1}=\frac{\eta}{\lambda f_2})} \\ n &= 1, 2, 3, 4, \end{aligned} \quad (13)$$

where f_2 is the focal length of L2 in Fig. 3. By substituting $x = -\frac{f_1}{f_2}\xi$ and $y = -\frac{f_1}{f_2}\eta$, E_3^n can be rewritten as

$$E_3^1 = 3A + B + C + D, \quad (14)$$

$$E_3^2 = 3A - B - C + D, \quad (15)$$

$$E_3^3 = 3A + B - C - D, \quad (16)$$

$$E_3^4 = 3A - B + C - D, \quad (17)$$

where

$$A = \frac{f_1^3}{4f_2^3} E_1(x, y),$$

$$B = \frac{f_1^3}{4f_2^3} E_1(x, y) \otimes \frac{1}{\pi^2 xy},$$

$$C = \frac{f_1^3}{4f_2^3} E_1(x, y) \otimes \frac{\delta(y)}{\pi x} i,$$

$$D = \frac{f_1^3}{4f_2^3} E_1(x, y) \otimes \frac{\delta(x)}{\pi y} i.$$

δ is the Dirac function, and \otimes denotes convolution. It can be seen that item A represents the original light field propagating without any diffraction, and B , C , and D are the diffraction

items. Item C represents the diffraction effect due to one edge. Item D is the diffraction effect due to another edge, and item B is the joint contribution of both edges. The diffraction effect will cause energy loss and also intensity fluctuation inside the detection pupil.

The intensity distributions of each measurement step are shown as follows:

$$\begin{aligned} I_3^1 &= |E_3^1|^2 = 9|A|^2 + |B|^2 + |C|^2 + |D|^2 \\ &\quad + 6 \text{Re}(\bar{A}B) + 6 \text{Re}(\bar{A}C) + 6 \text{Re}(\bar{A}D) \\ &\quad + 2 \text{Re}(\bar{B}C) + 2 \text{Re}(\bar{B}D) + 2 \text{Re}(\bar{C}D), \end{aligned} \quad (18)$$

$$\begin{aligned} I_3^2 &= |E_3^2|^2 = 9|A|^2 + |B|^2 + |C|^2 + |D|^2 \\ &\quad - 6 \text{Re}(\bar{A}B) - 6 \text{Re}(\bar{A}C) + 6 \text{Re}(\bar{A}D) \\ &\quad + 2 \text{Re}(\bar{B}C) - 2 \text{Re}(\bar{B}D) - 2 \text{Re}(\bar{C}D), \end{aligned} \quad (19)$$

$$\begin{aligned} I_3^3 &= |E_3^3|^2 = 9|A|^2 + |B|^2 + |C|^2 + |D|^2 \\ &\quad + 6 \text{Re}(\bar{A}B) - 6 \text{Re}(\bar{A}C) - 6 \text{Re}(\bar{A}D) \\ &\quad - 2 \text{Re}(\bar{B}C) - 2 \text{Re}(\bar{B}D) + 2 \text{Re}(\bar{C}D), \end{aligned} \quad (20)$$

$$\begin{aligned} I_3^4 &= |E_3^4|^2 = 9|A|^2 + |B|^2 + |C|^2 + |D|^2 \\ &\quad - 6 \text{Re}(\bar{A}B) + 6 \text{Re}(\bar{A}C) - 6 \text{Re}(\bar{A}D) \\ &\quad - 2 \text{Re}(\bar{B}C) + 2 \text{Re}(\bar{B}D) - 2 \text{Re}(\bar{C}D). \end{aligned} \quad (21)$$

The signals S'_x and S'_y are determined by calculating the intensity distributions of the four steps as follows:

$$\begin{aligned} S'_x &= I_{x+} - I_{x-} = I_4^2 + I_4^3 - I_4^1 - I_4^4 \\ &= -24 \text{Re}(\bar{A}C) - 8 \text{Re}(\bar{B}D), \end{aligned} \quad (22)$$

$$\begin{aligned} S'_y &= I_{y+} - I_{y-} = I_4^3 + I_4^4 - I_4^1 - I_4^2 \\ &= -24 \text{Re}(\bar{A}D) - 8 \text{Re}(\bar{B}C), \end{aligned} \quad (23)$$

where

$$\text{Re}(\bar{A}C) = -\frac{f_1^6 |u_0|^2}{4f_2^6 \pi} \int_{-P(y)}^{P(y)} \frac{\sin \left\{ \frac{2\pi}{\lambda} [\varphi(x, y) - \varphi(x', y)] \right\}}{x - x'} dx'$$

$$\begin{aligned} \text{Re}(\bar{B}D) &= \frac{f_1^6 |u_0|^2}{4f_2^6 \pi^2} \int_{-P(x)}^{P(x)} dy_2 \int_{-y_0}^{y_0} dy_1 \int_{-P(y_2)}^{P(y_1)} \\ &\quad \times \frac{\sin \left\{ \frac{2\pi}{\lambda} [\varphi(x, y_2) - \varphi(x_1, y_1)] \right\}}{\pi^3 (x - x_1)(y - y_1)(y - y_2)} dx_1, \end{aligned}$$

$$\text{Re}(\bar{A}D) = -\frac{f_1^6 |u_0|^2}{4f_2^6 \pi} \int_{-P(y)}^{P(y)} \frac{\sin \left\{ \frac{2\pi}{\lambda} [\varphi(x, y) - \varphi(x, y')] \right\}}{y - y'} dy',$$

$$\begin{aligned} \text{Re}(\bar{B}C) &= \frac{f_1^6 |u_0|^2}{4f_2^6 \pi^2} \int_{-P(y)}^{P(y)} dy_2 \int_{-y_0}^{y_0} dy_1 \int_{-P(y_1)}^{P(y_2)} \\ &\quad \times \frac{\sin \left\{ \frac{2\pi}{\lambda} [\varphi(x_2, y) - \varphi(x_1, y_1)] \right\}}{\pi^3 (x - x_1)(y - y_1)(x - x_2)} dx_1. \end{aligned}$$

$\text{Re}(\bar{B}D)$ and $\text{Re}(\bar{B}C)$ represent the cross terms of the x and y directions, respectively. They do not affect the signs of the

signals, but their amplitude, as discussed in [15]. The diffraction theory shows that the SPWFS has the same response characteristics as PWFS. In particular, in the case of small aberrations, the output signal of the SPWFS is linear with the local tilt of wavefront, so it can work in a closed-loop system.

For the PWFS, if a similar 4f imaging system is used as shown in Fig. 4, the intensity distribution of four quarters on the detection plane can be written as

$$I_{\text{pyramid}}^1 = |A|^2 + |B|^2 + |C|^2 + |D|^2 - 2 \operatorname{Re}(\bar{A}B) - 2 \operatorname{Re}(\bar{A}C) - 2 \operatorname{Re}(\bar{A}D) + 2 \operatorname{Re}(\bar{B}C) + 2 \operatorname{Re}(\bar{B}D) + 2 \operatorname{Re}(\bar{C}D), \quad (24)$$

$$I_{\text{pyramid}}^2 = |A|^2 + |B|^2 + |C|^2 + |D|^2 + 2 \operatorname{Re}(\bar{A}B) + 2 \operatorname{Re}(\bar{A}C) - 2 \operatorname{Re}(\bar{A}D) + 2 \operatorname{Re}(\bar{B}C) - 2 \operatorname{Re}(\bar{B}D) - 2 \operatorname{Re}(\bar{C}D), \quad (25)$$

$$I_{\text{pyramid}}^3 = |A|^2 + |B|^2 + |C|^2 + |D|^2 - 2 \operatorname{Re}(\bar{A}B) + 2 \operatorname{Re}(\bar{A}C) + 2 \operatorname{Re}(\bar{A}D) - 2 \operatorname{Re}(\bar{B}C) - 2 \operatorname{Re}(\bar{B}D) + 2 \operatorname{Re}(\bar{C}D), \quad (26)$$

$$I_{\text{pyramid}}^4 = |A|^2 + |B|^2 + |C|^2 + |D|^2 + 2 \operatorname{Re}(\bar{A}B) - 2 \operatorname{Re}(\bar{A}C) + 2 \operatorname{Re}(\bar{A}D) - 2 \operatorname{Re}(\bar{B}C) + 2 \operatorname{Re}(\bar{B}D) - 2 \operatorname{Re}(\bar{C}D). \quad (27)$$

It can be seen that the intensity on SPWFS's detection plane is three times larger than the intensity of one pupil image on PWFS's detection plane. However, the diffraction energy of SPWFS is similar to PWFS, and so the diffraction effect of SPWFS is weaker than that of PWFS. Owing to weak diffraction, the light energy loss of SPWFS is less, and the intensity fluctuation is weaker. For a practical system, the signal-to-noise ratio (SNR) of the wavefront sensor is important. The APD array and CCD are two commonly used detection devices. For a certain APD array used, its SNR is only in proportion with the incident power under the shot-noise-limited condition. So a higher SNR SPWFS can be realized. However, if a CCD is used, the SNR should be analyzed strictly in consideration of the exposure limitation of SPWFS. For a CCD under a low illumination condition and with a short exposure time, the readout noise and shot noise will be the dominant noise sources. PWFS's SNR can be expressed as

$$\operatorname{SNR}_{\text{PWFS}}(n, m) = \frac{P(n, m)Q_e t}{\sqrt{P(n, m)Q_e t + N_r}}. \quad (28)$$

Q_e is the quantum efficiency, and N_r is the readout noise. Both will be constant if a certain kind of CCD is determined. n

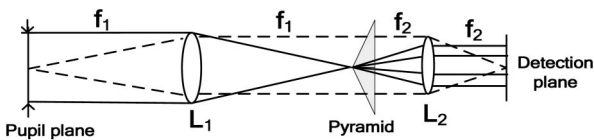


Fig. 4. Optical diagram of nonmodulation PWFS.

and m denote the subaperture index. P is the incident power, and t is the integration time. Due to the sequential operation method used, the exposure in each step of the SPWFS should be no longer than a quarter of the PWFS. If the diffraction effect and readout noise are ignored, the incident light power of the SPWFS is three times larger than that of the PWFS. So SPWFS's average SNR can be expressed as

$$\operatorname{SNR}_{\text{SPWFS}} = \frac{\sqrt{3}}{2} (\operatorname{SNR}_{\text{PWFS}}). \quad (29)$$

4. NUMERICAL SIMULATION

We simulate the wavefront sensing process of SPWFS based on the diffraction theory discussed above. Simulation parameters are selected as follows. The laser wavelength is 632.8 nm. The ratio of the focal length of f_1 to f_2 is 1. The aperture of the detection pupil is 8 mm in diameter and 350 pixels in one direction. The gap between each micromirror is 5 μm . If the input wavefront has no aberration, the normalized intensity distribution of each step on the detection plane of the SPWFS is as in Figs. 5(a)–5(d). We also simulate the PWFS using the same parameters. The pupil sizes and the focal lengths of the lenses are all the same. The difference is that the exposure of the PWFS is four times longer than that of the SPWFS so that the limitation of integration time caused by the sequential operation method of SPWFS can be taken into account appropriately. The normalized intensity distribution on the detection plane of PWFS is as in Fig. 5(e), where the pupil outlines are marked with red circles.

It can be seen from Fig. 5 that the light energy outside the pupil of the SPWFS is weaker than that of the PWFS. The results of quantitative computation have also been provided. The ratio of energy utilization of the SPWFS is 76.20%, whereas that of the PWFS is 40.34%. This means that almost 24% of energy goes out of the detection pupil of SPWFS due to the diffraction effect, and it is more than 59% of energy for PWFS. So the average SNR of SPWFS will be 1.63 times higher than that of PWFS if the energy loss is taken into account. If the incident wavefront has aberration, the situation will be changed somewhat. Simulation results are provided in Fig. 6, which reports the SNR ratio of SPWFS to PWFS when the incident has aberrations composed of four to 120 Zernike modes following the Kolmogorov power spectrum. In the simulation, we calculate the energy loss of SPWFS and PWFS first when the incident wavefront aberration has a different RMS

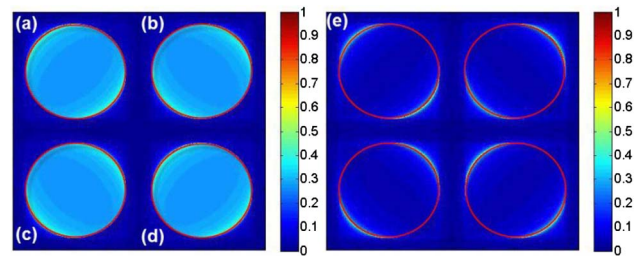


Fig. 5. (a)–(d) Light intensity distributions of steps 1–4 on the SPWFS's detection plane. (e) That on the PWFS's detection plane when the input wavefront has no aberration.

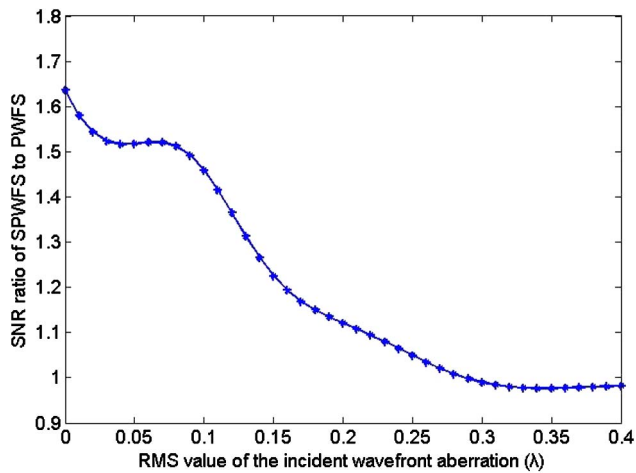


Fig. 6. SNR ratio of SPWFS to PWFS as a function of the amplitude of incident aberration.

value, and the effective power ratio of SPWFS to PWFS is calculated. Then the SNR ratio can be calculated based on Eq. (28). If the SNR ratio is larger than 1.0, SPWFS has higher average SNR than PWFS. It can be seen that the ratio will decrease with the increase of aberration, and SPWFS can realize a higher average SNR in the case of small aberration.

The noise equivalent angle (NEA) is another important parameter for slope-based wavefront sensors. The NEA for PWFS is given by

$$\text{NEA}_{\text{PWFS}} = \frac{1/g(n, m)}{\text{SNR}_{\text{PWFS}(n, m)}}, \quad (30)$$

where n and m denote the subaperture index and g is the centroid gain. Meanwhile, the NEA for SPWFS is given by

$$\text{NEA}_{\text{SPWFS}} = \frac{3/g(n, m)}{\text{SNR}_{\text{SPWFS}(n, m)}}. \quad (31)$$

The factor of 3 comes from scaling in the gradient calculation [see Eqs. (5) and (6)].

If the calculated average SNR is substituted and the incident wavefront has no aberration, it can be seen from Eqs. (30) and (31) that the average NEA of PWFS is about 1.84 times higher than that of SPWFS for a given system configuration. It should be pointed out that although SPWFS has higher average SNR, PWFS has better NEA performance.

It can also be seen from Fig. 5 that the intensity distribution of SPWFS has less fluctuation. The standard deviation of energy, as the definition of the light energy fluctuation, inside the detection pupil of SPWFS is 0.09, and that of PWFS is 0.36. This means a smoother energy distribution of SPWFS. So the probability of saturation or insufficiency of intensity on the detector plane of SPWFS is lower than that of PWFS if the average light power is the same. For a practice system, the pixels with too high or low gray level will degrade the systems' performance, and the closed-loop adaptive optics system may be unstable.

The simulation results of SPWFS and PWFS for a series of Zernike modes ($Z(2, 0)$, $Z(2, -2)$, $Z(3, -1)$, $Z(3, -3)$, $Z(4, 0)$ with $\text{RMS} = 0.1\lambda$) are shown in Figs. 7–11. The

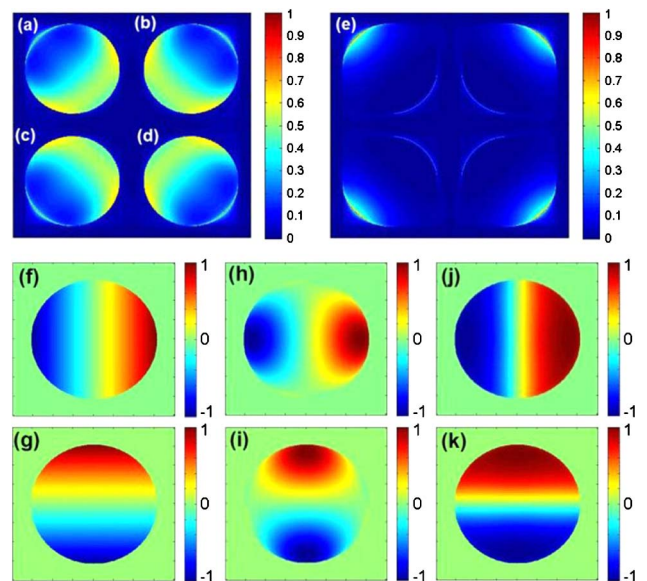


Fig. 7. Local tilt sensing results of the $Z(2, 0)$ Zernike polynomial using SPWFS and PWFS.

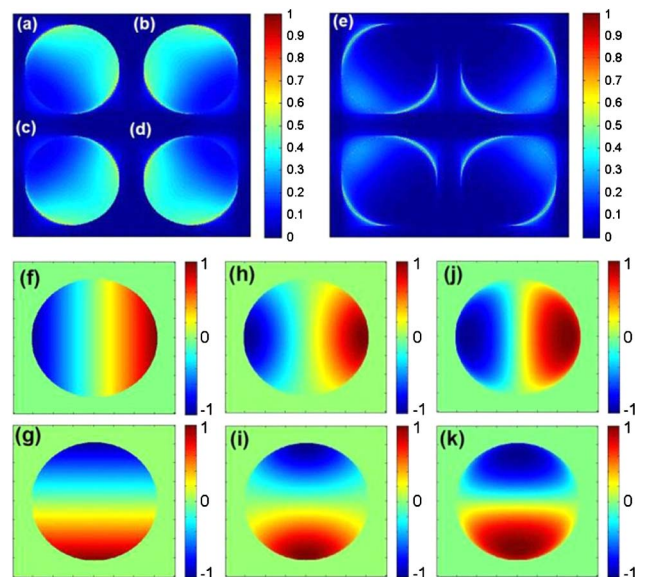


Fig. 8. Local tilt sensing results of the $Z(2, -2)$ Zernike polynomial using SPWFS and PWFS.

Zernike order is as in [16]. Parts (a), (b), (c), and (d) in each figure show the intensity distribution the SPWFS's detection plane in each detection step, and part (e) is that on the PWFS's detection plane. Parts (f) and (g) show the gradients of the wavefront. Parts (h) and (i) show the output signals of the SPWFS given by Eqs. (5) and (6). Parts (j) and (k) show the output signals of the PWFS given by Eqs. (1) and (2).

The simulation figures (shown from Figs. 7 to 11) show similar characteristics of local tilt sensing results measured by nonmodulation SPWFS and PWFS. Both have some discrepancies with the real wavefront derivative caused by the

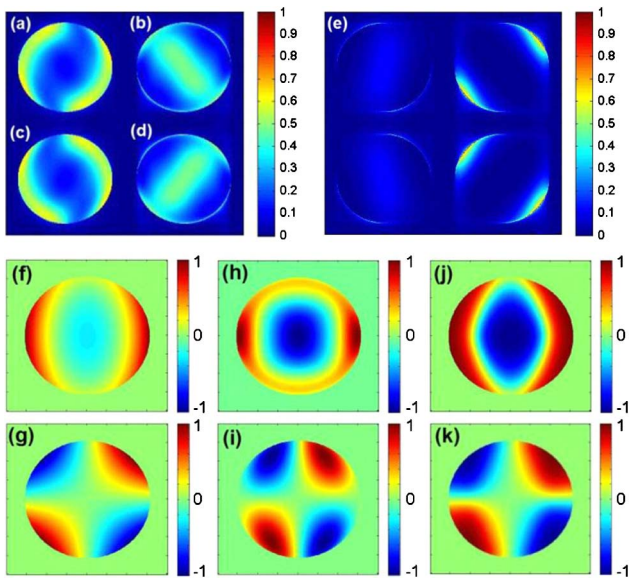


Fig. 9. Local tilt sensing results of the $Z(3, -1)$ Zernike polynomial using SPWFS and PWFS.

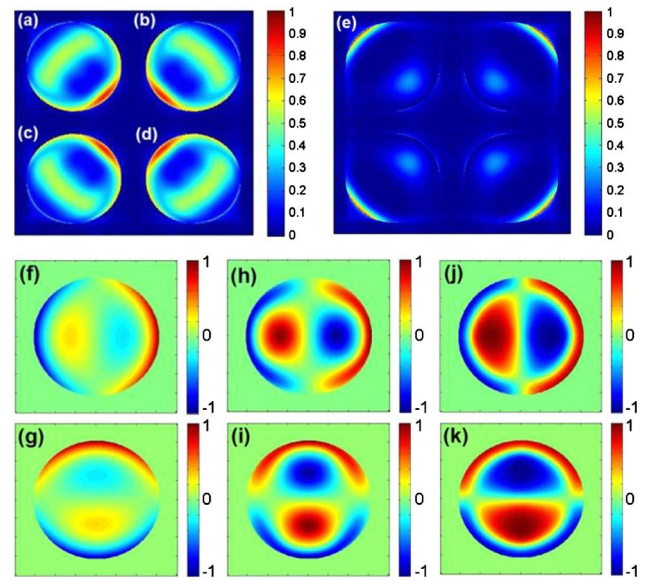


Fig. 11. Local tilt sensing results of the $Z(4, 0)$ Zernike polynomial using SPWFS and PWFS.

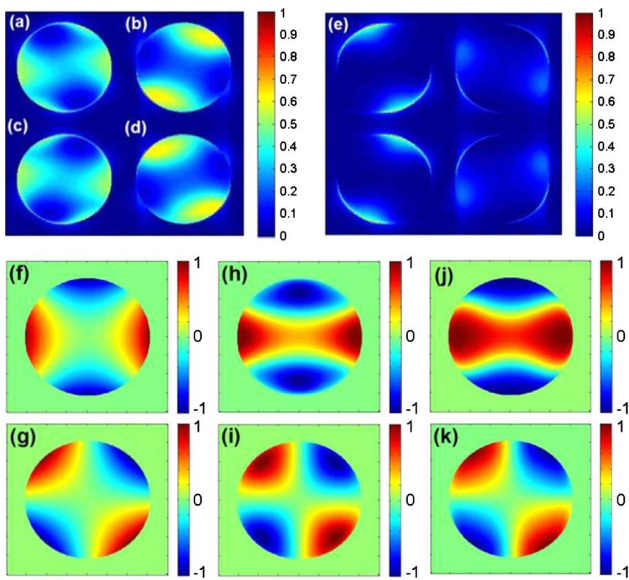


Fig. 10. Local tilt sensing results of the $Z(3, -3)$ Zernike polynomial using SPWFS and PWFS.

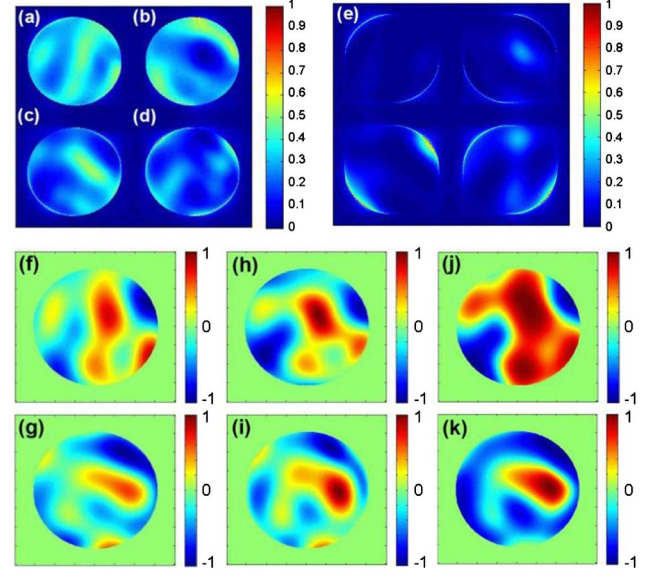


Fig. 12. Local tilt sensing results of the Kolmogorov phase screen using SPWFS and PWFS.

saturation effect due to the small linear range. However, the outlines of the local tilt sensing signal of SPWFS and PWFS are identical to the real wavefront derivative, and the sign distributions of the wavefront slope have negligible differences from those of the real wavefront derivative.

For a general description of the characteristics, the simulation figures of the Kolmogorov phase screen are shown in Fig. 12 with $RMS = 0.1\lambda$ composed of four to 65 Zernike modes.

The simulation results of the Kolmogorov phase screen also show that the SPWFS has identical characteristics to the PWFS

and the right sign distribution of local wavefront tilt can be detected by nonmodulation SPWFS and PWFS. From the conclusions proposed in [15], a wavefront sensor can work correctly in a closed-loop iteration system if the measured signal trend is coincident with the true signal trend, and a non-modulation PWFS can be used in a closed-loop adaptive optics system.

In the following simulation, SPWFS is also used in a closed-loop correction system. It is assumed that the wavefront corrector can compensate measured aberration with no error. Wavefront distortion, composed of four to 120 Zernike modes,

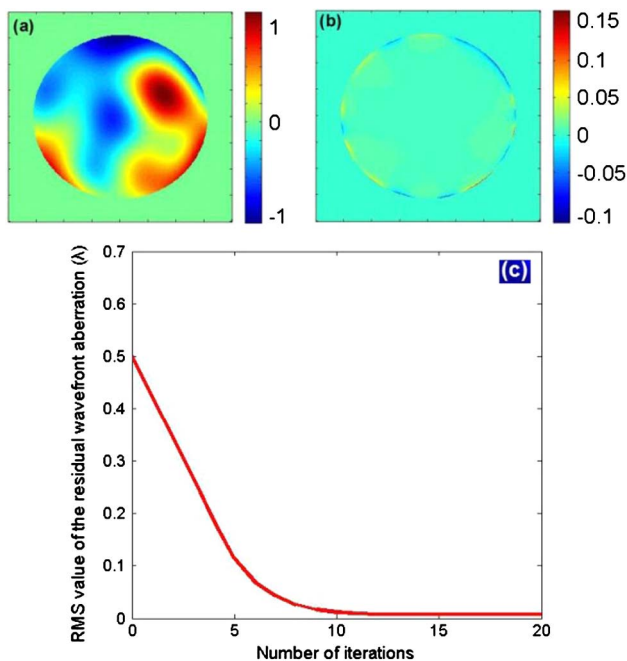


Fig. 13. (a), (b) Initial and corrected wavefront. (c) Evolution of RMS with closed-loop correction.

of 0.5λ in RMS value and with the Kolmogorov power spectrum, is loaded as the original wavefront, as shown in Fig. 13(a). When the closed-loop adaptive optics system reaches a steady state, the RMS value of the residual aberration is 0.015λ as shown in Fig. 13(b). A plot of the RMS value for the residual aberration is provided in Fig. 13(c). More correction results of the Kolmogorov phase screen with different D/r_0 values (D is the input aperture diameter, and r_0 is the Fried parameter) are provided in Fig. 14.

It is clear that the closed-loop wavefront correction using the nonmodulation SPWFS is feasible although there is a lot of work to do for applying it into a practical adaptive optics system. In a practical system, the micromirror array should

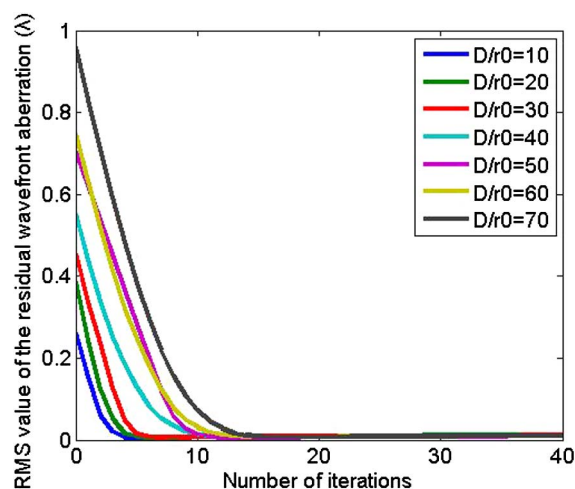


Fig. 14. Plot of the RMS for different aberrations following Kolmogorov phase spectrum.

be selected carefully. First, its performance should be fast enough so that the wide detection bandwidth can be realized. Second, the gap between micromirrors should be small enough for high light utilization, and for degrading the influence of artifacts.

The commercial micromirror array with 256×256 tilt mirrors provided by Fraunhofer IPMS based on micro electrical–mechanical system (MEMS) technology may be a good choice, and of course a custom one is an option. The time sequence relationship between the tilting of the micromirror and the exposure of the CCD (same as the readout of the APD array) must be exact, ensuring that the micromirror is in an exact tilt angle at the time of exposure.

5. CONCLUSIONS AND FUTURE WORK

In this paper, a sequential operation approach of a pyramid sensor, which is based on a micromirror array, is described. Theory calculation and simulation analysis have shown that SPWFS has very similar characteristics to PWFS, and nonmodulation SPWFS can also be used in a closed-loop adaptive optics system. Furthermore, SPWFS has some advantages. First, owing to the reflective micromirror array used, SPWFS can be used in a broadband optical system easily, without specific achromatic design. Second, the detection element with one-fourth pixels of SPWFS can realize the same wavefront resolution as PWFS, which means higher uniformity of sensitivity and lower cost, especially for the APD array. Third, the relay system design of SPWFS would be simplified compared with PWFS. Fourth, SPWFS has a weaker diffraction effect and a smoother light energy distribution.

In future work, an experimental validation using a custom-made micromirror array is planned for 2015, and an on-sky demonstration is planned in 2016.

REFERENCES

1. G. Rousset, "Wave-front sensors," in *Adaptive Optics in Astronomy*, F. Roddier, ed. (Cambridge University, 1999), pp. 91–130.
2. K. Yao, J. Wang, X. Liu, and W. Liu, "Closed-loop adaptive optics system with a single liquid crystal spatial light modulator," *Opt. Express* **22**, 17216–17226 (2014).
3. R. Ragazzoni, "Pupil plane wavefront sensing with an oscillating prism," *J. Mod. Opt.* **43**, 289–293 (1996).
4. R. Ragazzoni, A. Ghedina, A. Baruffolo, E. Marchetti, J. Farinato, T. Niero, G. Crimi, and M. Ghigo, "Testing the pyramid wavefront sensor on the sky," *Proc. SPIE* **4007**, 423–430 (2000).
5. S. Esposito, A. Tozzi, A. Puglisi, E. Pinna, A. Richardi, S. Busoni, L. Busoni, P. Stefanini, M. Xompero, D. Zanotti, and F. Pieralli, "First light AO system for LBT: toward on-sky operation," *Proc. SPIE* **6272**, 62720A (2006).
6. M. Feldt, D. Peter, S. Hippler, T. Henning, J. Aceituno, and M. Goto, "PYRAMIR: first on-sky results from an infrared pyramid wavefront sensor," *Proc. SPIE* **6272**, 627218 (2006).
7. R. Ragazzoni and J. Farinato, "Sensitivity of a pyramidal wave front sensor in closed loop adaptive optics," *Astron. Astrophys.* **350**, 23–26 (1999).
8. T. Y. Chew, R. M. Clare, and R. G. Lane, "A comparison of the Shack–Hartmann and pyramid wavefront sensors," *Opt. Commun.* **268**, 189–195 (2006).
9. S. E. Egner, W. Gaessler, R. Ragazzoni, B. LeRoux, T. M. Herbst, J. Farinato, E. Diolaiti, and C. Arcidiacono, "MANU-CHAO: a laboratory ground-layer adaptive optics experiment," *Proc. SPIE* **6272**, 62724X (2006).

10. S. Esposito, E. Pinna, A. Puglisi, A. Tozzi, and P. Stefanini, "Pyramid sensor for segmented mirror alignment," *Opt. Lett.* **30**, 2572–2574 (2005).
11. H. W. Babcock, "The possibility of compensating astronomical seeing," *Publ. Astron. Soc. Pac.* **65**, 229–236 (1953).
12. A. Wang, J. Yao, P. Cai, and H. Ren, "Design and fabrication of pyramid wavefront sensor," *Opt. Eng.* **49**, 073401 (2010).
13. A. Burvall, E. Daly, S. R. Chamot, and C. Dainty, "Linearity of the pyramid wavefront sensor," *Opt. Express* **14**, 11925–11934 (2006).
14. S. Wang, C. Rao, H. Xian, J. Zhang, J. Wang, and Z. Liu, "Laboratory demonstrations on a pyramid wavefront sensor without modulation for closed-loop adaptive optics system," *Opt. Express* **19**, 8135–8150 (2011).
15. J. Wang, F. Bai, Y. Ning, L. Huang, and S. Wang, "Comparison between non-modulation four-sided and two-sided pyramid wavefront sensor," *Opt. Express* **18**, 27534–27549 (2010).
16. M. A. A. Neil, M. J. Booth, and T. Wilson, "New modal wave-front sensor: a theoretical analysis," *J. Opt. Soc. Am. A* **17**, 1098–1107 (2000).